

Large scale scattering using fast solvers based on neural operators

Zongren Zou^{a,1}, Adar Kahana^{a,1}, Enrui Zhang^a, Eli Turkel^b, Rishikesh Ranade^c, Jay Pathak^c,
George Em Karniadakis^{a,d,2}

^a*Division of Applied Mathematics, Brown University, Providence, RI 02906, USA*

^b*Department of Applied Mathematics, Tel Aviv University, Tel Aviv 69978, Israel*

^c*CTO Office, Ansys Inc, Canonsburg, PA 15317, USA*

^d*School of Engineering, Brown University, Providence, RI 02906, USA*

Abstract

We extend a recently proposed machine-learning-based iterative solver, i.e. the hybrid iterative transferable solver (HINTS), to solve the scattering problem described by the Helmholtz equation in an exterior domain with a complex absorbing boundary condition. The HINTS method combines neural operators (NOs) with standard iterative solvers, e.g. Jacobi and Gauss-Seidel (GS), to achieve better performance by leveraging the spectral bias of neural networks. In HINTS, some iterations of the conventional iterative method are replaced by inferences of the pre-trained NO. In this work, we employ HINTS to solve the scattering problem for both 2D and 3D problems, where the standard iterative solver fails. We consider square and triangular scatterers of various sizes in 2D, and a cube and a model submarine in 3D. We explore and illustrate the extrapolation capability of HINTS in handling diverse geometries of the scatterer, which is achieved by training the NO on non-scattering scenarios and then deploying it in HINTS to solve scattering problems. The accurate results demonstrate that the NO in HINTS method remains effective without retraining or fine-tuning it whenever a new scatterer is given. Taken together, our results highlight the adaptability and versatility of the extended HINTS methodology in addressing diverse scattering problems.

Keywords: Scientific machine learning, wave scattering, Helmholtz equation, neural operator, DeepONet

¹These two authors contributed equally.

²Corresponding author: george_karniadakis@brown.edu (George Em Karniadakis).

1. Introduction

In recent years, there has been a paradigm shift in solving computationally scientific problems. The introduction of scientific machine learning (SciML) has unlocked a large variety of new methods for solving partial differential equations (PDEs) including linear and non-linear systems of equations, forward and inverse problems [1]. Most of these methods attempt to replace the traditional solver with ones based on modern machine learning (ML) techniques. However, the effectiveness of such SciML methods has been non-uniform across different problems, especially those with multiscale characteristics. On the other hand, traditional solvers may offer some special attributes and high-accuracy solutions, e.g. for problems with high-frequency content at a relatively low cost. Hence, it may be beneficial to explore *hybrid* methods, combining classical methods with ML to create uniformly powerful solvers that exploit the strengths of both fields. In this work, we develop such a hybrid method and tackle one of the most challenging tasks in numerical analysis: solving the scattering problem with various geometries of the scatterer in 2D and in 3D settings. The governing equation is the Helmholtz equation, which, in general, is not positive-definite, and includes complex-valued boundary conditions that destroy the symmetry.

One of the most popular SciML approaches proposed recently to tackle PDEs is the physics-informed neural network (PINN) [2], which embeds the governing equations (physics, chemistry, biology, etc.) [3–14] into the loss function of a neural network (NN). This makes the network aware of the physics while training, and captures the solution when the training converges. PINN is an example of the replacement of conventional numerical solvers since they obtain the sought solution of a PDE by training NNs without invoking any classical solver. Another category is operator learning [15–22], where one uses NNs to approximate the solution operator of a family of solutions of a PDE via learning the mapping between functions. Examples include mapping material properties to a PDE solution, a future state to an initial condition (solving an inverse problem), one state variable to another, etc. The big advantage of such neural operators (NOs) is that, once trained, the network can infer solutions in real-time, without the need for re-training. Hence, NOs are also aimed at replacing a solver.

Herein, we consider an important physical problem, namely the wave scattering problem [23–27]. It involves an incoming wavefront, coming from infinity and projected into the domain, hitting a solid obstacle, which is referred to as the scatterer. The impact creates scattered waves that propagate through the domain. The scattering problem poses many challenges and thus has been studied by many authors. One challenge is that for high wavenumbers the problem is non-symmetric positive definite, which means it cannot be solved using many classical solvers including Jacobi (J) and Gauss-Seidel (GS) [28]. The shifted Laplacian [29] and other similar approaches have been suggested to overcome this issue, but each proposed method has its pros and cons. Another challenge is working with complex absorbing boundary conditions, such as the Sommerfeld type [30]. Implementations of boundary conditions of this type display a trade-off between efficiency (of implementation and computational optimization) and accuracy (rate of absorption). Last, dealing with scatterers that have complex geometries is still an open problem. Most current methods require solving from scratch when changing the scatterer geometry. Some authors suggest treating the problem as a boundary value problem, defined by the boundary of the scatterer

[31] but there are still several limitations of all such methods.

The classical methods for solving the Helmholtz scattering problem, as well as many other PDE and related problems, are iterative methods using the finite elements (FE) or finite differences (FD) approximations. The PDE is first discretized on a mesh or a grid, and then a system of equations is assembled to solve the discretized problem. Many methods for solving the system have been proposed over time, ranging from the most classical Jacobi or GS, through multigrid methods (geometric or algebraic) [32, 33], preconditioning [34, 35], etc. These methods compete in computational complexity, execution speed, and robustness. Decades of research has led to the development of innovative algorithms that excel in solving those problems. However, there are still open problems and issues that even the most advanced solvers struggle with.

An important recent development is the hybrid iterative numerical transferable solver (HINTS) [36]. The hybrid property of the HINTS refers to the combination of both a classical iterative solver with a neural operator (NO). The basis of the algorithm is as follows: after the assembly of the system, in each iteration of the solver we either invoke a classical solver, e.g. the Jacobi method [28], or the NO solver. This is intuitively effective because the classical solvers are well known to handle high-frequency errors well, but struggle with the low-frequency modes. In contrast, the machine-learning-based methods such as NOs are exactly the opposite (attributing to a phenomenon called the spectral bias of neural networks [37]). By combining the two we obtain the best of both worlds.

In this work, we tackle and solve difficult scattering problems using HINTS. We formulate the problem mathematically, including a Sommerfeld-type boundary condition, an arbitrary scatterer inside the domain with a reflecting boundary condition, an incoming wavefront from one of the boundary edges, etc. We then assemble the complex system of equations, train a NO that is part of the HINTS, and use it in HINTS to solve the problem efficiently. We show results with different scatterers, observing the robustness and efficiency of the method, in both 2D and 3D scenarios.

The paper is organized as follows: in Section 2, we present the problem formulation, and in Section 3 we present the methodology. In Section 4 we present the computational results in 2D and 3D, including scattering from a submarine, and in Section 5 we conclude with a summary.

2. Problem Formulation

The problem consists of a domain Ω , with a scatterer inside the domain $\Omega_{scat} \subset \Omega$. The scatterer is assumed to be perfectly reflecting and have a homogeneous Dirichlet boundary condition. An incoming wave, denoted as g , is projected onto the domain from one of the sides, denoted as $\partial\Omega_{inc}$ (in this work, the top boundary), where a Neumann boundary condition is imposed. The other edges, denoted as $\partial\Omega_{ABC}$, are open boundaries, using a Sommerfeld absorbing boundary condition [30, 38–40]. The general complex Helmholtz

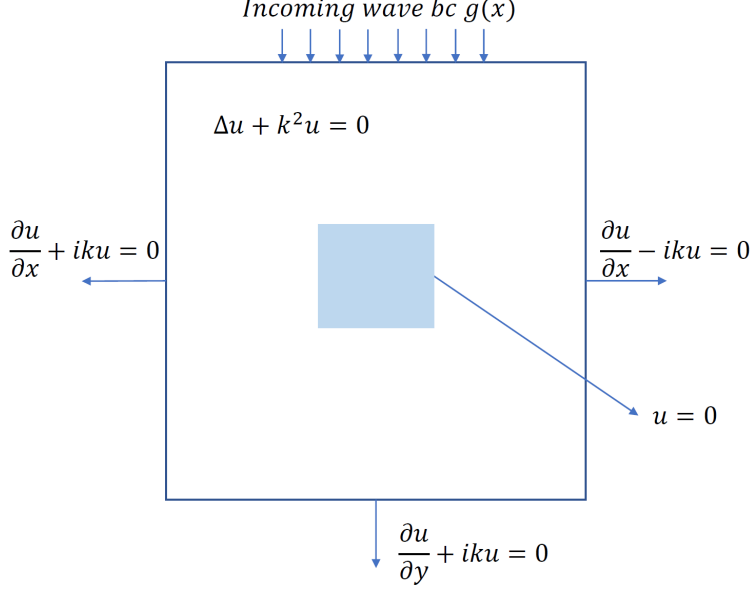


Figure 1: Setup of a standard scattering problem. The scatterer is illustrated by the shaded area in the middle of the domain. The upper boundary condition creates an incoming wavefront, while the other three boundary conditions are absorbing ones. Inside the domain, we solve the complex Helmholtz equation. The boundary of the scatterer is set as a reflecting boundary using a homogeneous Dirichlet condition.

problem formulation for this setup is given by:

$$\Delta u(\vec{x}) + k(\vec{x})^2 u(\vec{x}) = f(\vec{x}), \quad \vec{x} \in \Omega \subset \mathbb{R}^d, \quad (1a)$$

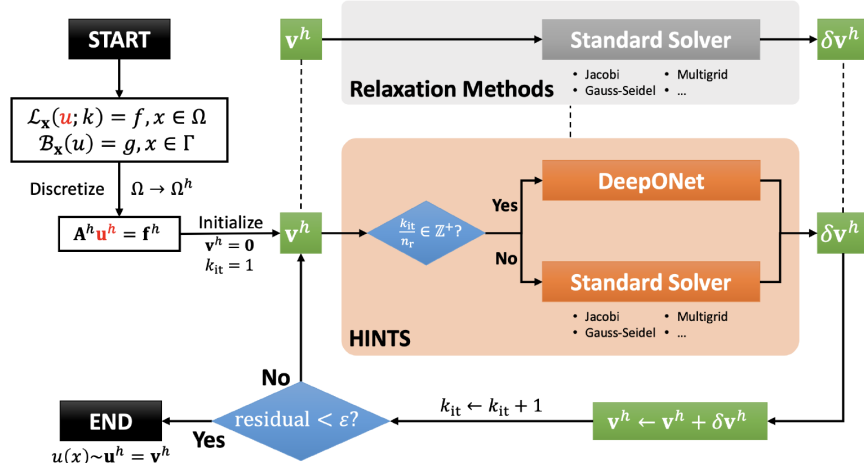
$$\frac{\partial u(\vec{x})}{\partial \mathbf{n}(\vec{x})} - ik(\vec{x})u(\vec{x}) = 0, \quad \vec{x} \in \partial\Omega_{ABC}, \quad (1b)$$

$$\frac{\partial u(\vec{x})}{\partial \mathbf{n}(\vec{x})} = g(\vec{x}), \quad \vec{x} \in \partial\Omega_{inc}, \quad (1c)$$

$$u(\vec{x}) = 0, \quad \vec{x} \in \Omega_{scat} \subset \Omega, \quad (1d)$$

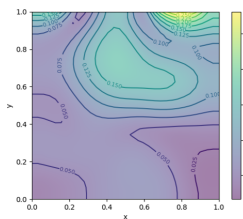
where $k(\vec{x})$ denotes the real space-dependent wave number and $f(\vec{x})$ denotes the complex space-dependent forcing term. An illustration of the problem in two dimensions is given in Fig. 1, where the domain Ω is a square and the forcing term is set to zero. The dynamics of the system is introduced by the incoming wave $g(\vec{x})$ (assumed real). The scatterer is taken to be a rectangle in this figure but we will consider diverse 2D and 3D scatterers in the following.

In this work, we consider the scattering problem described by the above complex Helmholtz equation in both 2D and 3D cases. In 2D cases, we consider a square domain $\Omega = [0, 1]^2 \ni \vec{x} = [x, y]^T$ and use a second-order finite difference scheme with five-point stencil to approximate the derivatives. The system is discretized on a uniform mesh. In the 3D cases, we consider a cubic domain $\Omega = [0, 1]^3 \ni \vec{x} = [x, y, z]^T$ and employ the second-order finite difference scheme with a uniform mesh. The details of the numerical discretization are presented in Appendix A. Without loss of generality, we set the forcing term f to zero for the physical problem we solve in our experiments. However, to stabilize and accelerate the iterative solver, the forcing term is not zero in training the neural operators for HINTS. We will discuss this in more detail in Section 3.



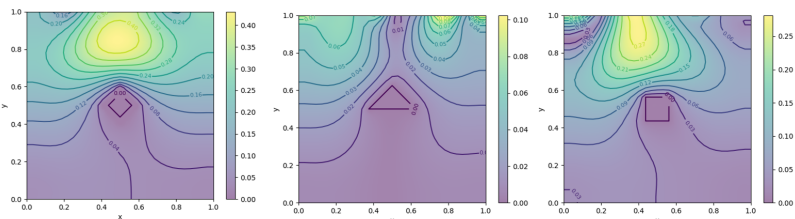
(a) HINTS.

The NO is trained on:



Extrapolate →

HINTS solves:



(b) Extrapolation of HINTS.

Figure 2: In (a), we present the schematic view of HINTS; adapted from [36]. DeepONets are chosen as the backbone for the neural operator (NO) employed in HINTS. In (b), we highlight that in this work, the extrapolation capability of HINTS is utilized to solve the scattering problem. In particular, the NO employed in HINTS is trained on non-scattering problems to learn the solution operator of the complex Helmholtz equation, while HINTS solves the scattering problem with different geometries of the scatterer, without re-training or fine-tuning the NO when a new scatterer is given.

3. Methodology

In this section, we discuss the methodology used to solve the scattering problem, i.e. the hybrid iterative numerical transferable solver (HINTS) [36]. The HINTS method combines a standard iterative solver, e.g. Jacobi and Gauss-Seidel (GS) [28, 41], with neural operators (NOs) [15, 16, 18, 19, 22, 42, 43] to improve the convergence of the iterative solver by leveraging the spectral bias of neural operators [36, 44]. A schematic view of the HINTS method is presented in Fig. 2(a). Some iterations of the standard iterative solver are replaced with the inference of the pre-trained NO. For example, as shown in Fig. 2, the NO, which is a DeepONet [15], is applied once for every n_r iterations of the standard solver. Interested readers are directed to [36] for more details.

The NO employed in HINTS is trained beforehand to approximate the solution operator of certain parametric PDEs. Then, the fast online inference is enabled when the NO is invoked in the iterative solver. Intuitively, the PDE whose solution operator is approximated by the

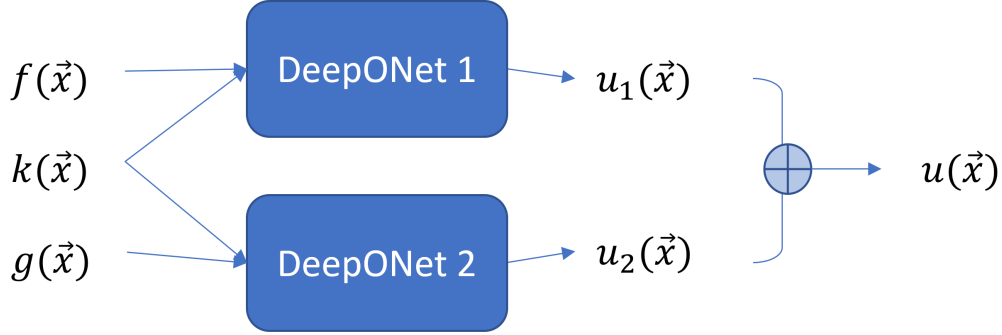


Figure 3: The architecture of the neural operator (NO) employed in HINTS to solve the scattering problem. The proposed NO consists of two DeepONets: DeepONet 1 learns the solution operator of Eq. (1) with a zero incoming wave, while DeepONet 2 learns the solution operator of Eq. (1) with a zero forcing term. Based on the linearity, we can superimpose the two solutions to obtain the total solution to the complex Helmholtz equation defined in Eq. (1): $u = u_1 + u_2$. We note that $g(\vec{x})$ is defined only on the boundary.

NO should be the same as the PDE targeted by the iterative solver, because NOs trained in this way encode the physics correctly and can provide accurate inference when invoked in HINTS. For the scattering problem, the NO should be trained to learn the solution operator \mathcal{G} that maps the wave number k , the forcing term f , and the incoming wave g to the sought solution of Eq. 1 with Ω_{scat} known and fixed, which describes the scattering problem with the scatterer defined as Ω_{scat} :

$$\mathcal{G} : k, f, g \mapsto u \text{ s.t. Eq. (1) is satisfied.} \quad (2)$$

We note that here k, f, g are space-dependent functions. This implies that for the effective application of HINTS, a new NO must be trained each time a new scatterer is given so that the NO utilized in HINTS accurately captures the solution operator of the new scattering problem. This constrains the versatility of HINTS in addressing diverse scatterer configurations, e.g. different geometries of the scatterer. However, we leverage the extrapolation capability of NOs (specifically DeepONets) and use HINTS to solve PDEs that are different from the one on which the NO is trained. In particular, as illustrated in Fig. 2(b), the NO is trained on non-scattering problems and learns the solution operator of Eq. (1) with $\Omega_{scat} = \emptyset$, to solve scattering problems with various geometries of the scatterer. The details of the experimental setup will be discussed in Section 4.

We employ the DeepONet as the backbone for the NO to approximate the solution operator; see [15] for details on DeepONet. An issue with the formulation presented in Eq. (1) is that the incoming wave (from the upper boundary) g dictates the dynamics of the system, which are otherwise zero. Therefore, classical HINTS training as suggested in [36] is not possible for this case. In addition, in the scenario where we have $f \equiv 0$ and $g \neq 0$, there may be large non-smooth jumps in the right-hand side between the first upper row (in the two-dimensional case) or the first upper plane (in the three-dimensional case), and the second row or plane respectively. This discontinuity is difficult to handle when approximating the solution operator of Eq. (1) with a single DeepONet, which operates on the lower frequencies. Moreover, the standard numerical solver (that is not susceptible to these issues) creates residuals with jumps, which cannot be easily handled by DeepONets: even if a DeepONet

was trained well for the initial scenario, it is expected to fail in later iterations. Therefore, we utilize the linearity of the problem and construct the NO with two DeepONets: one to address the forcing term f , referred to as DeepONet 1, and the other to address the incoming wave g , referred to as DeepONet 2. Specifically, as displayed in Fig. 3, DeepONet 1 takes as input k and f and outputs u_1 while DeepONet 2 takes as input k and g and outputs u_2 . This decomposition allows a separate learning of two PDEs: DeepONet 1 for Eq. (1) with a zero incoming wave $g(\vec{x}) = 0, \vec{x} \in \partial\Omega_{inc}$, and DeepONet 2 for Eq. (1) with a zero forcing term $f(\vec{x}) = 0, \vec{x} \in \Omega$. The solution to the entire complex Helmholtz equation is then obtained by superposition, i.e., $u = u_1 + u_2$. We note that DeepONet 1 predicts the correction to the approximated solution based on the current residual of the forcing term f , and DeepONet 2 predicts it based on the current residual of the boundary term g .

4. Results

We present test results of using HINTS to solve the scattering problem described by the Helmholtz equation (1) with a complex absorbing boundary condition. We test the methodology on 2D cases in Section 4.1, and 3D cases in Section 4.2. Both a finite difference scheme and a direct solver [45–49] for linear systems are employed to obtain the reference solution and generate data for training NOs. Details of the solver, including the discretization and a verification test can be found in Appendix A and Appendix B, respectively. In all the numerical experiments, we use double precision and the Jacobi iterative method [28] as the backbone iterative solver. We stress that our methodology can be integrated with any iterative solvers [36].

4.1. 2D scattering problems

We solve the 2D scattering problem on a square domain $\Omega := [0, 1]^2$. The approximate Sommerfeld boundary condition, $\frac{\partial u}{\partial n} + iku = 0$, is imposed on the left, right and bottom boundaries, while a Neumann boundary condition is imposed on the top boundary, i.e. $\frac{\partial u}{\partial n}(x) = g(x), x \in \partial\Omega$, and a Dirichlet boundary condition is imposed on the scatterer, denoted by Ω_{scat} . Unless stated otherwise, we discretize the domain uniformly with a 33×33 mesh, set the incoming wave $g(x) = \sin(3\pi x), x \in [0, 1]$ and the forcing term $f(x, y) = 0, x, y \in [0, 1]$. We randomly sample the wave number $k(x, y)$ from a 2D Gaussian random field with mean 6.0 and the following squared exponential kernel function:

$$K(\vec{x}, \vec{x}') = s^2 \exp\left(-\frac{\|\vec{x} - \vec{x}'\|^2}{2l^2}\right), \vec{x}, \vec{x}' \in \Omega, \quad (3)$$

where s^2 is the variance and is set to 0.5, l denotes the correlation length and is set to 0.3, and $\|\cdot\|$ denotes the ℓ_2 vector norm. We stress that this approach applies to any discretization and incoming wave function.

We first consider a square scatterer of size 0.125×0.125 (5×5 in the mesh points) centered at $(x, y) = (0.5, 0.5)$. The randomly generated wave number $k(x, y)$ and the reference solution are displayed in Fig. 4(a) and Fig. 4(b). The standard Jacobi method fails to solve this scattering problem (as shown in Fig. 4(c)) because we are addressing a non-symmetric and non-positive-definite problem: there are in total 121 out of 1089 (around 11.1%) eigenvalues of the LHS matrix with negative real parts, resulting in a non-positive-definite matrix. In

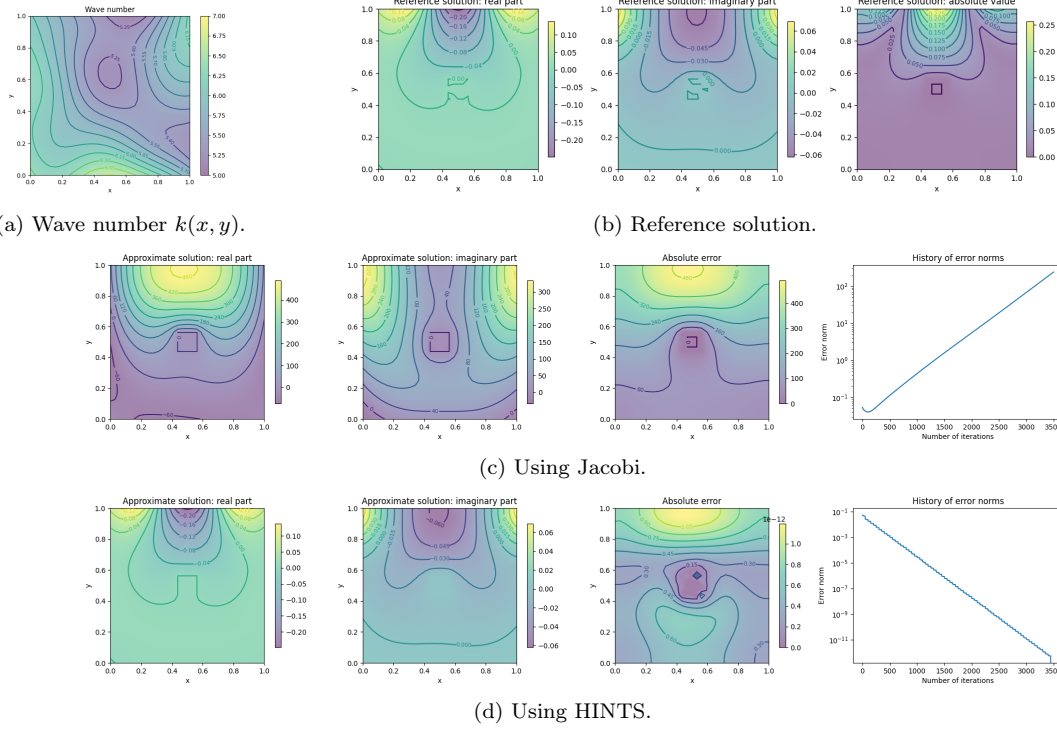


Figure 4: Comparison between using the standard Jacobi method (in (c)) and using the HINTS (in (d)) in solving the 2D scattering problem on $[0, 1]^2$ with a square scatterer (of size 0.125×0.125) placed at the center of the domain. Note that the NO employed in HINTS is trained on non-scattering problems and approximates the solution operator of Eq. (1) with $\Omega_{scat} = \emptyset$.

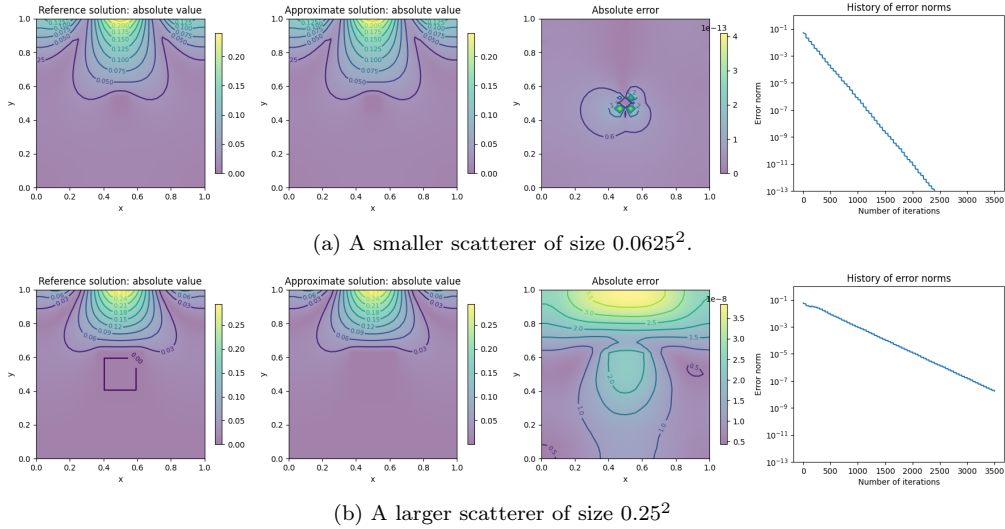


Figure 5: Results of HINTS in solving the 2D scattering problem with square scatterers of different sizes. Note that the NO is trained on non-scattering problems. By comparing with Fig. 4(d) in which a square scatterer of size 0.125^2 is considered, we notice the degradation in performance of HINTS as the size of the scatterer increases.

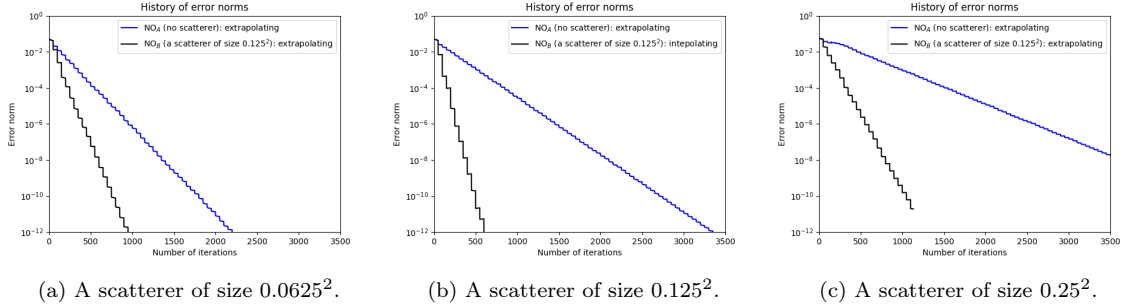


Figure 6: Comparison of error norms between two different neural operators (NOs) employed in HINTS for solving the scattering problem with a square scatterer of different sizes. The first NO (NO_A) is trained on the non-scattering problem (blue curves) and the second (NO_B) is trained on the scattering problem with the square scatterer of size 0.125^2 (black curves). Note that NO_B is interpolating in the scattering problem with the scatterer of size 0.125^2 .

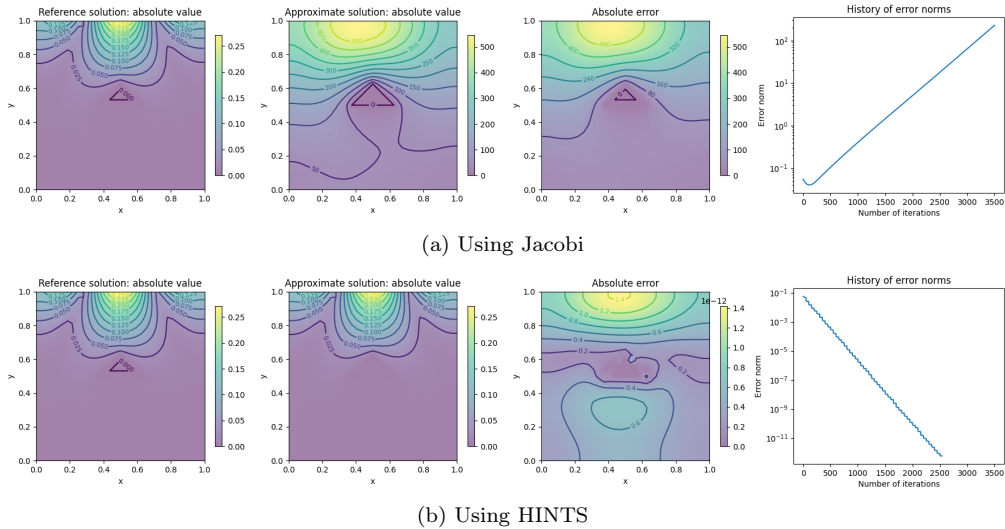


Figure 7: Comparison between using the standard Jacobi method and using the HINTS in solving the 2D scattering problem with a triangular scatterer (the coordinates of its vertices are $(0.375, 0.5)$, $(0.625, 0.5)$, and $(0.5, 0.625)$).

contrast, HINTS can solve this problem with an accuracy to machine precision, as shown in Fig. 4(d). The NO is applied once for every 50 iterations in HINTS.

The NO employed in HINTS approximates the solution operator of Eq. 1, which maps the wave number k , the (non-zero) complex forcing term f , and the incoming wave g to its sought solution u . However, the NO is trained to learn the solution operator of the 2D Helmholtz equation without the scatterer in which $\Omega_{scat} = \emptyset$, and used in HINTS to solve the scattering problem in which $\Omega_{scat} \neq \emptyset$. Specifically, the training data of the NO are obtained from solving Eq. (1) while ignoring the scatterer and its associated Dirichlet boundary condition using randomly generated samples of k , f , and g . The details of the data generation, the architecture of DeepONets, and the training are given in Appendix C. The success of HINTS in solving the scattering problem with a NO trained to solve non-scattering ones demonstrates the high flexibility and the extrapolation capability of our approach.

4.1.1. Scatterers of different sizes

We next test HINTS in solving the scattering problem with a square scatterer of different sizes. We consider a smaller square scatterer of size 0.0625^2 and a larger one of size 0.25^2 . For comparisons, the wave number $k(x, y)$, incoming wave $g(x)$, and the neural operator employed in HINTS remain the same as in the previous case. The neural operator is trained on non-scattering problems and applied once every 50 iterations. The results are presented in Fig. 5, from which we see that the HINTS method succeeds in solving the scattering problem in both cases. The number of eigenvalues with negative real parts is 106 (10%) and 177 (16%) in the smaller and larger scatterer cases, respectively. By comparing with the results shown in Fig. 4(d), we observe the degradation in the convergence rate of HINTS as the size of the scatterer increases: the larger the scatterer, the slower HINTS converges. This is because the NO is trained on non-scattering problems, which is different from the problem we solve using the iterative method. As the dissimilarity between the problem on which the NO is trained and the one tackled by HINTS grows (the size of the scatterer increases), it poses greater challenges for HINTS (essentially the NO) to extrapolate. For a sufficiently large scatterer, HINTS no longer converges since it is too far from the training set which has no scatterer.

However, this issue can be alleviated by employing a NO trained on similar scattering problems. In this example, we conduct a comparison between using two differently trained NOs in HINTS to solve the scattering problem with a square scatterer of different sizes. The first NO, referred to as NO_A , is the same as in the previous case, i.e. trained on non-scattering problems, while the second NO, referred to as NO_B , both share the same architecture and are instead trained on scattering problems with a square scatterer of size 0.125^2 . The details of the training of NO_B can be found in Appendix C. We test HINTS with these two NOs in three different cases: (1) a square scatterer with size 0.0625^2 , (2) a square scatterer with size 0.125^2 , and (3) a square scatterer with size 0.25^2 . NOs are applied once for every 50 iterations. We note that NO_A is extrapolating in all three cases while NO_B is interpolating in Case (2) and extrapolating in Cases (1) and (3). The comparison is presented in Fig. 6. We see that the convergence of HINTS with NO_A becomes slower as the size of the scatterer increases, which makes the extrapolation more difficult. The performance can be improved significantly by employing a NO trained on more similar scattering problems. HINTS with NO_B achieves the fastest convergence in Case (2) because in this case, HINTS (and NO_B) is interpolating: the problem HINTS solves is the same as the one on which NO_B is trained.

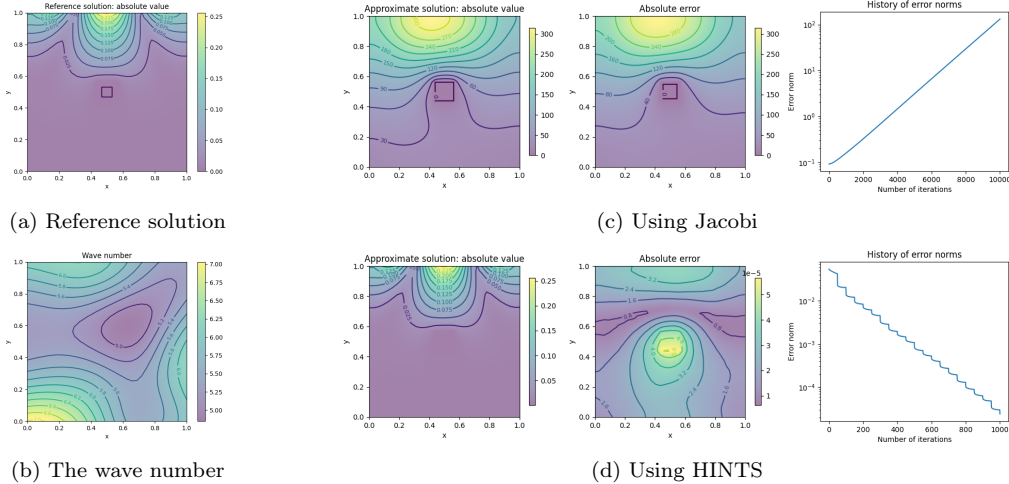


Figure 8: Using HINTS to solve the scattering problem discretized on a 65×65 uniform mesh, while the NO employed in HINTS is trained on a 33×33 uniform mesh.

4.1.2. A scatterer of different shape

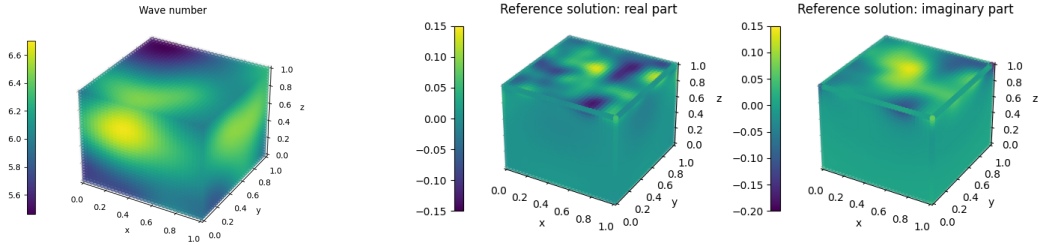
We next consider a scatterer with a different geometry. Specifically, we solve the scattering problem with a triangular scatterer, placed at the center of the domain and defined by the coordinates of its three vertices: $(0.375, 0.5)$, $(0.625, 0.5)$, and $(0.5, 0.625)$. We test HINTS with the same wave number $k(x, y)$ and incoming wave $g(x)$. The NO is chosen as the one trained on non-scattering problems as in previous cases. The comparison between the standard Jacobi method and HINTS is presented in Fig. 7. We observe a similar divergence of Jacobi and convergence of HINTS as in the square scatterer case.

4.1.3. A different mesh

We close our study of 2D scattering problems by demonstrating the mesh invariance of HINTS. In all the previous cases, the mesh used to generate data for training NOs on non-scattering problems is the same as the one used to solve scattering problems, i.e. a $33 \times 33 \times 33$ uniform mesh. Now, we consider a $65 \times 65 \times 65$ uniform mesh in solving the scattering problem using HINTS but with the same NO as in the previous case, which is trained to solve non-scattering problems on the smaller mesh. This is achieved by interpolating $k(x, y)$ and the residuals of the PDE and the boundary condition between the different meshes whenever the NO is called. We consider a square scatterer of size 0.125^2 , use a different wavenumber $k(x, y)$ and a different incoming wave $g(x)$, randomly sampled from 2D and 1D GRFs (see Appendix C for details), respectively, and further increase the number of iterations to 10,000 for better performance. In HINTS, the neural operator solver is applied once every 200 iterations. The comparison between the standard Jacobi method and HINTS is displayed in Fig. 8. Even though the NO employed in HINTS is trained on a different mesh, HINTS produces solutions accurate to machine precision. The mesh-invariant nature of HINTS enables the reuse of the already-trained NO across mesh variations.

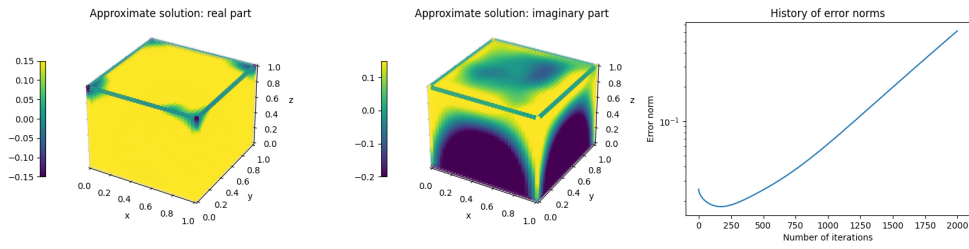
4.2. 3D scattering problems

In this subsection, we solve the 3D scattering problem on a cubic domain $\Omega := [0, 1]^3$. The Sommerfeld boundary condition is imposed on the front, back, left, right, and bottom

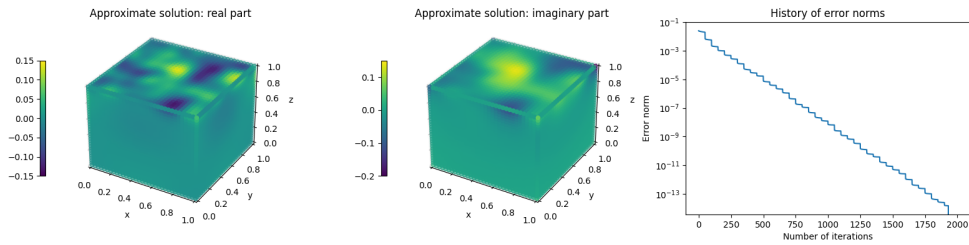


(a) Wave number $k(x, y, z)$.

(b) Reference solution.



(c) Using Jacobi.



(d) Using HINTS.

Figure 9: Comparison between using the standard Jacobi method (in (c)) and using the HINTS (in (d)) in solving the 3D scattering problem on $[0, 1]^3$ with a cubic scatterer (with size 0.125^3) placed at the center. (a) shows the 3D wave number $k(x, y, z)$ and (b) shows the reference solution. Note that we discretize the domain with a $33 \times 33 \times 33$ uniform mesh, while the NO in HINTS is trained on 3D non-scattering problems with a $17 \times 17 \times 17$ uniform mesh.

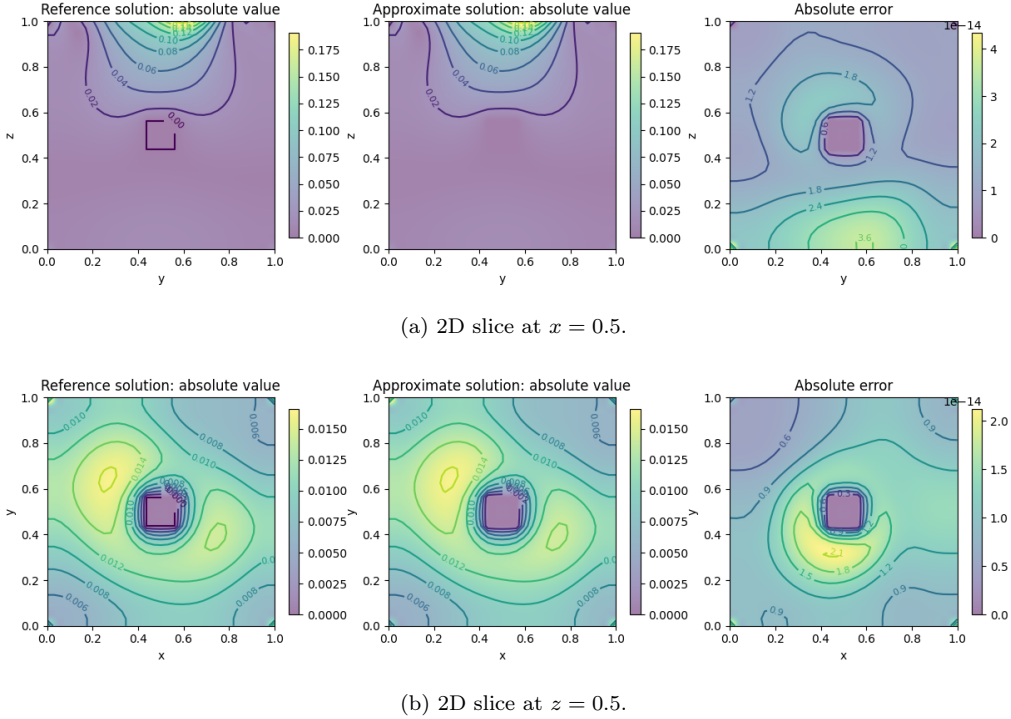


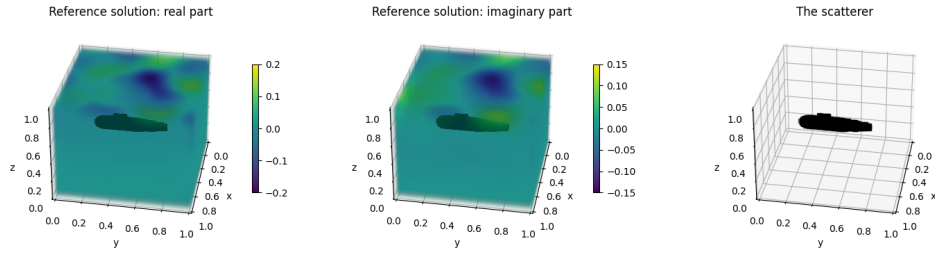
Figure 10: 2D slices of the solution from using HINTS to solve the 3D scattering problem with a cube scatterer. The absolute values of the solution are shown.

boundaries of Ω , a Neumann boundary condition with an incoming wave $g(x, y)$ is imposed on the top boundary, and a Dirichlet boundary condition is imposed on the scatterer. The wave number $k(x, y, z)$ (displayed in Fig. 9(a)) and the incoming wave $g(x, y)$ are randomly sampled from the 3D GRF with mean 6.0 and kernel function (3) with $l = 0.3$ and $s = 0.2$ and the 2D GRF with mean zero and kernel function (3) with $l = 0.1$ and $s = 1.0$, respectively. The forcing term is set to zero.

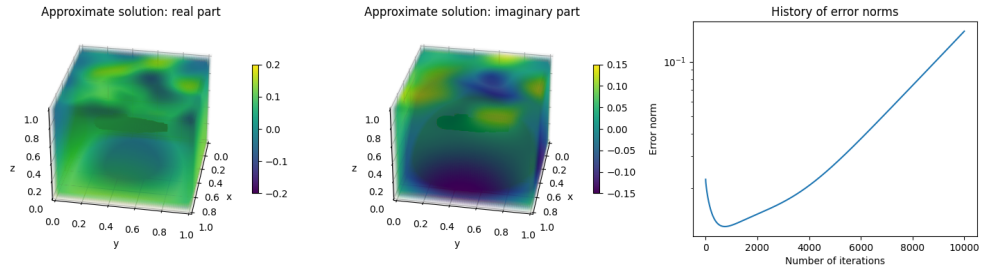
We first consider a cube scatterer of size 0.125^3 , placed at the center of the domain. In this case, we discretize the domain with a $33 \times 33 \times 33$ uniform mesh and solve the scattering problem using the standard Jacobi method and HINTS for 2,000 iterations. We present the comparison in Fig. 9 and 2D slices of the sought solution ($u|_{x=0.5}$ and $u|_{z=0.5}$) in Fig. 10. Thus, the HINTS method yields the solution in high accuracy for the 3D scattering problem while the standard Jacobi method diverges. The NO employed in HINTS is trained on 3D non-scattering problems and a $17 \times 17 \times 17$ uniform mesh, and is applied once every 50 iterations.

4.2.1. A submarine-shaped scatterer

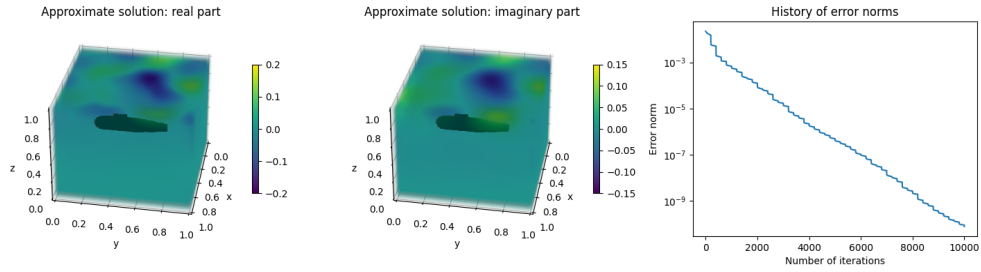
We next solve the 3D scattering problem with a submarine-like scatterer. The submarine has been modeled with Computer Aided Design (CAD) software. The model is not of a classified operational submarine but captures the general shape. The code used to parse the model from the CAD software can be used for the classified models. The model features the body of the submarine, as well as a fin on top of it. Focusing only on the NO part of the HINTS, we do not use a mesh to represent the submarine, but rather we use a staircasing



(a) Reference solution and the submarine geometry (rightmost).

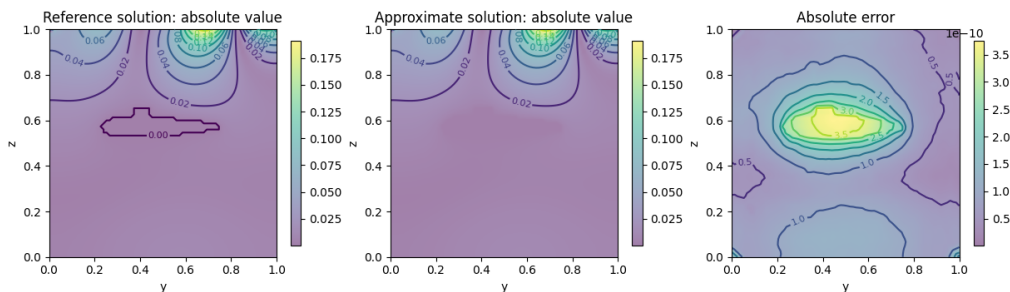


(b) Using Jacobi.

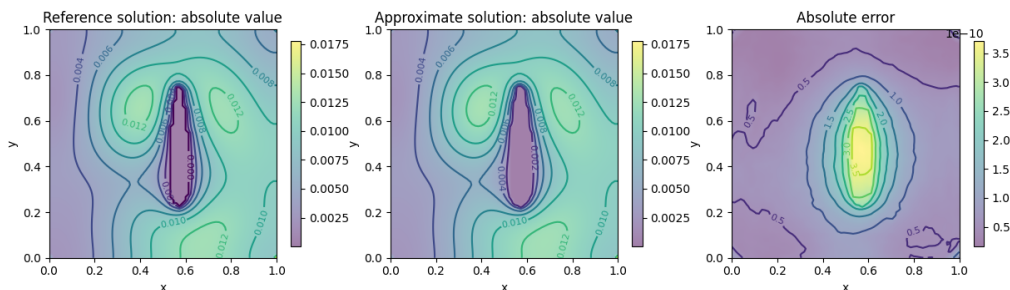


(c) Using HINTS.

Figure 11: Solving the 3D scattering problem with a submarine scatterer using the standard Jacobi method (in (b)) and HINTS (in (c)). The submarine scatterer is rescaled to fit the domain and displayed at the rightmost of (a). We discretize the domain with a $76 \times 76 \times 76$ uniform mesh, while the NO in HINTS is trained on 3D non-scattering problems with a $17 \times 17 \times 17$ uniform mesh.



(a) 2D Slice at $x = 0.5733$.



(b) 2D Slice at $z = 0.5733$.

Figure 12: 2D slices of the solution from using HINTS to solve the 3D scattering problem with a submarine scatterer. The absolute values of the solution are shown.

technique with a uniform grid, where we assign the value 1 to nodes within the submarine geometry and 0 otherwise. As the NO interpolates the space, in addition to tackling only the low-frequency modes, this is a sufficient assumption for achieving satisfactory results in this case. Thus, the NO can scale with the size of the problem of interest. We scale the submarine to fit the domain $[0, 1]^3$; see Fig. 11(a). We discretize the domain with a $76 \times 76 \times 76$ uniform mesh. The wave number and the incoming wave are the same as in the previous case but interpolated linearly for the new mesh. We employ the same NO in HINTS, which is trained on 3D non-scattering problems with the $17 \times 17 \times 17$ uniform mesh, and apply it once every 200 iterations. This is because when we move to a significantly larger problem (in terms of the number of elements) we also have more high-frequency modes. As suggested in [36], we invoke the NO application only after the classical solver smooths the high-frequency modes well enough. A premature application means that the NO faces high-frequency errors that it is not capable of handling, causing the NO to fail and return an even higher error causing the overall iteration process to diverge. The optimal NO to classical solver ratio is problem-specific and experiments show that more elements result in a larger ratio. The results for the scattering HINTS with the submarine geometry are shown in Fig. 11, in which the standard Jacobi method and HINTS are employed for 10,000 iterations. The standard Jacobi method fails to yield an accurate solution while HINTS converges. We also present 2D slices of the sought solution ($u|_{x=0.5733}$ and $u|_{z=0.5733}$) using HINTS in Fig. 12, from which we see that HINTS accurately solves the 3D scattering problem with the submarine scatterer.

5. Summary

We explored the capability of HINTS in solving the scattering problem described by the Helmholtz equation in an exterior domain with a complex absorbing boundary condition, for which a standard iterative solver, e.g. Jacobi, fails. We consider both 2D and 3D cases and observe the convergence of HINTS and the divergence of the standard iterative solver. The latter is caused by the non-positive definiteness of the discretized system. We overcome this by combining the pre-trained neural operators (NOs) [15, 16, 19], specifically DeepONets, with the standard iterative solver and thus leveraging their spectral bias. We then solve scattering problems across diverse scatterer geometries in a fast and accurate manner.

One possible limitation of using pretrained NOs to solve partial differential equations (PDEs) is that a new NO must be trained each time we solve a new family of PDEs. For example, when the size or shape of the scatterer changes in the scattering problem, the NO needs to be retrained from scratch or at least fine-tuned to provide accurate inferences for the new problem. However, since the contribution of NOs in HINTS is primarily decreasing the errors of the low-frequency modes [36, 44], HINTS demonstrates resilience against this limitation. In this work, we mainly focus on investigating the extrapolation capability of the NO in HINTS in tackling different scatterers. To this end, we examine the scenario where the PDE, whose solution operator is approximated by the NO, differs from the one HINTS aims to solve. Specifically, we first train the NO on the non-scattering problem, which is described by the complex Helmholtz equation without the scatterer, and then employ HINTS to solve the scattering problem with the scatterer in different shapes, including squares of different sizes and triangles in 2D cases, and cube and a scaled submarine in 3D cases. We have presented significant evidence showcasing the effectiveness of HINTS in dealing with such challenges, demonstrating the extrapolation capability and versatility of HINTS in addressing different scatterers. However, there is a degradation of performance when applying HINTS to solve the scattering problem when the NO is trained on non-scattering ones. As the problem with a scatterer becomes further removed from the case of no scattering the convergence rate decreases and may even stop converging. Also, the degradation depends on the wave number k . This issue can be mitigated by training a NO on more similar scattering problems.

Acknowledgements

We acknowledge the support of the MURI/AFOSR FA9550-20-1-0358 project and the DOE-MMICS SEA-CROGS DE-SC0023191 award. G.E.K. is supported by the ONR Vannevar Bush Faculty Fellowship (N00014-22-1-2795). We also acknowledge support from Ansys Inc. We thank Professor Sergey Petropavlovsky from HSE University for his contribution in extracting the CAD model of the submarine.

References

- [1] George Em Karniadakis, Ioannis G Kevrekidis, Lu Lu, Paris Perdikaris, Sifan Wang, and Liu Yang. Physics-informed machine learning. *Nature Reviews Physics*, 3(6):422–440, 2021.
- [2] Maziar Raissi, Paris Perdikaris, and George E Karniadakis. Physics-informed neural networks: A deep learning framework for solving forward and inverse problems involving nonlinear partial differential equations. *Journal of Computational physics*, 378:686–707, 2019.
- [3] Shengze Cai, Zhiping Mao, Zhicheng Wang, Minglang Yin, and George Em Karniadakis. Physics-informed neural networks (PINNs) for fluid mechanics: A review. *Acta Mechanica Sinica*, 37(12):1727–1738, 2021.
- [4] Shengze Cai, Zhicheng Wang, Sifan Wang, Paris Perdikaris, and George Em Karniadakis. Physics-informed neural networks for heat transfer problems. *Journal of Heat Transfer*, 143(6):060801, 2021.
- [5] Zhiping Mao, Ameya D Jagtap, and George Em Karniadakis. Physics-informed neural networks for high-speed flows. *Computer Methods in Applied Mechanics and Engineering*, 360:112789, 2020.
- [6] Guofei Pang, Lu Lu, and George Em Karniadakis. fPINNs: Fractional physics-informed neural networks. *SIAM Journal on Scientific Computing*, 41(4):A2603–A2626, 2019.
- [7] Kevin Linka, Amelie Schäfer, Xuhui Meng, Zongren Zou, George Em Karniadakis, and Ellen Kuhl. Bayesian physics informed neural networks for real-world nonlinear dynamical systems. *Computer Methods in Applied Mechanics and Engineering*, 402:115346, 2022.
- [8] Zhen Zhang, Zongren Zou, Ellen Kuhl, and George Em Karniadakis. Discovering a reaction–diffusion model for Alzheimer’s disease by combining PINNs with symbolic regression. *Computer Methods in Applied Mechanics and Engineering*, 419:116647, 2024.
- [9] Zongren Zou and George Em Karniadakis. L-HYDRA: Multi-head physics-informed neural networks. *arXiv preprint arXiv:2301.02152*, 2023.
- [10] Zongren Zou, Xuhui Meng, and George Em Karniadakis. Correcting model misspecification in physics-informed neural networks (PINNs). *Journal of Computational Physics*, page 112918, 2024.
- [11] Minglang Yin, Zongren Zou, Enrui Zhang, Cristina Cavinato, Jay D Humphrey, and George Em Karniadakis. A generative modeling framework for inferring families of biomechanical constitutive laws in data-sparse regimes. *Journal of the Mechanics and Physics of Solids*, 181:105424, 2023.
- [12] Paula Chen, Tingwei Meng, Zongren Zou, Jérôme Darbon, and George Em Karniadakis. Leveraging multitime Hamilton–Jacobi PDEs for certain scientific machine learning problems. *SIAM Journal on Scientific Computing*, 46(2):C216–C248, 2024.

- [13] Paula Chen, Tingwei Meng, Zongren Zou, Jérôme Darbon, and George Em Karniadakis. Leveraging Hamilton-Jacobi PDEs with time-dependent Hamiltonians for continual scientific machine learning. *arXiv preprint arXiv:2311.07790*, 2023.
- [14] Zongren Zou, Tingwei Meng, Paula Chen, Jérôme Darbon, and George Em Karniadakis. Leveraging viscous hamilton-jacobi pdes for uncertainty quantification in scientific machine learning. *arXiv preprint arXiv:2404.08809*, 2024.
- [15] Lu Lu, Pengzhan Jin, Guofei Pang, Zhongqiang Zhang, and George Em Karniadakis. Learning nonlinear operators via DeepONet based on the universal approximation theorem of operators. *Nature machine intelligence*, 3(3):218–229, 2021.
- [16] Zongyi Li, Nikola Borislavov Kovachki, Kamyar Azizzadenesheli, Burigede liu, Kaushik Bhattacharya, Andrew Stuart, and Anima Anandkumar. Fourier neural operator for parametric partial differential equations. In *International Conference on Learning Representations*, 2021.
- [17] Sifan Wang, Hanwen Wang, and Paris Perdikaris. Learning the solution operator of parametric partial differential equations with physics-informed DeepONets. *Science advances*, 7(40):eabi8605, 2021.
- [18] Nikola Kovachki, Zongyi Li, Burigede Liu, Kamyar Azizzadenesheli, Kaushik Bhattacharya, Andrew Stuart, and Anima Anandkumar. Neural operator: Learning maps between function spaces with applications to PDEs. *Journal of Machine Learning Research*, 24(89):1–97, 2023.
- [19] Lu Lu, Xuhui Meng, Shengze Cai, Zhiping Mao, Somdatta Goswami, Zhongqiang Zhang, and George Em Karniadakis. A comprehensive and fair comparison of two neural operators (with practical extensions) based on fair data. *Computer Methods in Applied Mechanics and Engineering*, 393:114778, 2022.
- [20] Oded Ovadia, Adar Kahana, Panos Stinis, Eli Turkel, and George Em Karniadakis. Vito: Vision transformer-operator. *arXiv preprint arXiv:2303.08891*, 2023.
- [21] Oded Ovadia, Eli Turkel, Adar Kahana, and George Em Karniadakis. Ditto: Diffusion-inspired temporal transformer operator. *arXiv preprint arXiv:2307.09072*, 2023.
- [22] Zongren Zou, Xuhui Meng, and George Em Karniadakis. Uncertainty quantification for noisy inputs-outputs in physics-informed neural networks and neural operators. *arXiv preprint arXiv:2311.11262*, 2023.
- [23] Alvin Bayliss and Eli Turkel. Radiation boundary conditions for wave-like equations. *Communications on Pure and applied Mathematics*, 33(6):707–725, 1980.
- [24] Eli Turkel and A Yefet. Absorbing pml boundary layers for wave-like equations. *Applied Numerical Mathematics*, 27(4):533–557, 1998.

- [25] Eli Turkel, Dan Gordon, Rachel Gordon, and Semyon Tsynkov. Compact 2d and 3d sixth order schemes for the helmholtz equation with variable wave number. *Journal of Computational Physics*, 232(1):272–287, 2013.
- [26] JA Ogilvy. Wave scattering from rough surfaces. *Reports on Progress in Physics*, 50(12):1553, 1987.
- [27] Alexander G Voronovich. *Wave scattering from rough surfaces*, volume 17. Springer Science & Business Media, 2013.
- [28] Yousef Saad. *Iterative methods for sparse linear systems*. SIAM, 2003.
- [29] Yogi A Erlangga, Cornelis Vuik, and Cornelis Willebrordus Oosterlee. On a class of preconditioners for solving the helmholtz equation. *Applied Numerical Mathematics*, 50(3-4):409–425, 2004.
- [30] Arnold Sommerfeld. *Partial differential equations in physics*. Academic press, 1949.
- [31] Christopher Davis, June G Kim, Hae-Soo Oh, and Min Hyung Cho. Meshfree particle methods in the framework of boundary element methods for the helmholtz equation. *Journal of Scientific Computing*, 55:200–230, 2013.
- [32] William L Briggs, Van Emden Henson, and Steve F McCormick. *A multigrid tutorial*. SIAM, 2000.
- [33] Wolfgang Hackbusch. *Multi-grid methods and applications*, volume 4. Springer Science & Business Media, 2013.
- [34] James H Bramble, Joseph E Pasciak, and Jinchao Xu. Parallel multilevel preconditioners. *Mathematics of computation*, 55(191):1–22, 1990.
- [35] Gabriele Ciaramella and Martin J Gander. *Iterative methods and preconditioners for systems of linear equations*. SIAM, 2022.
- [36] Enrui Zhang, Adar Kahana, Eli Turkel, Rishikesh Ranade, Jay Pathak, and George Em Karniadakis. A hybrid iterative numerical transferable solver (HINTS) for PDEs based on deep operator network and relaxation methods. *arXiv preprint arXiv:2208.13273*, 2022.
- [37] Nasim Rahaman, Aristide Baratin, Devansh Arpit, Felix Draxler, Min Lin, Fred Hamprecht, Yoshua Bengio, and Aaron Courville. On the spectral bias of neural networks. In *International conference on machine learning*, pages 5301–5310. PMLR, 2019.
- [38] Asaf Zarmi and Eli Turkel. A general approach for high order absorbing boundary conditions for the Helmholtz equation. *Journal of Computational Physics*, 242:387–404, 2013.
- [39] Alvin Bayliss, Max Gunzburger, and Eli Turkel. Boundary conditions for the numerical solution of elliptic equations in exterior regions. *SIAM Journal on Applied Mathematics*, 42(2):430–451, 1982.

- [40] H Gan, PL Levin, and Reinhold Ludwig. Finite element formulation of acoustic scattering phenomena with absorbing boundary condition in the frequency domain. *The Journal of the Acoustical Society of America*, 94(3):1651–1662, 1993.
- [41] Jinchao Xu. Iterative methods by space decomposition and subspace correction. *SIAM review*, 34(4):581–613, 1992.
- [42] Apostolos F Psaros, Xuhui Meng, Zongren Zou, Ling Guo, and George Em Karniadakis. Uncertainty quantification in scientific machine learning: Methods, metrics, and comparisons. *Journal of Computational Physics*, 477:111902, 2023.
- [43] Zongren Zou, Xuhui Meng, Apostolos F Psaros, and George E Karniadakis. NeuralUQ: A comprehensive library for uncertainty quantification in neural differential equations and operators. *SIAM Review*, 66(1):161–190, 2024.
- [44] Adar Kahana, Enrui Zhang, Somdatta Goswami, George Karniadakis, Rishikesh Ranade, and Jay Pathak. On the geometry transferability of the hybrid iterative numerical solver for differential equations. *Computational Mechanics*, 72(3):471–484, 2023.
- [45] Gilbert Strang. *Linear algebra and its applications*. 2012.
- [46] Timothy A Davis, John R Gilbert, Stefan I Larimore, and Esmond G Ng. Algorithm 836: Colamd, a column approximate minimum degree ordering algorithm. *ACM Transactions on Mathematical Software (TOMS)*, 30(3):377–380, 2004.
- [47] Timothy A Davis, John R Gilbert, Stefan I Larimore, and Esmond G Ng. A column approximate minimum degree ordering algorithm. *ACM Transactions on Mathematical Software (TOMS)*, 30(3):353–376, 2004.
- [48] Charles R. Harris, K. Jarrod Millman, Stéfan J. van der Walt, and et. al. Array programming with NumPy. *Nature*, 585(7825):357–362, September 2020.
- [49] Pauli Virtanen, Ralf Gommers, Travis E. Oliphant, and et. al. SciPy 1.0: Fundamental Algorithms for Scientific Computing in Python. *Nature Methods*, 17:261–272, 2020.
- [50] Diederik P Kingma and Jimmy Ba. Adam: A method for stochastic optimization. *arXiv preprint arXiv:1412.6980*, 2014.
- [51] Adam Paszke, Sam Gross, Francisco Massa, Adam Lerer, James Bradbury, Gregory Chanan, Trevor Killeen, Zeming Lin, Natalia Gimelshein, Luca Antiga, et al. Pytorch: An imperative style, high-performance deep learning library. *Advances in neural information processing systems*, 32, 2019.

Appendix A. Details of the discretization

For 2D cases, we discretize the system with a uniform mesh of size $(N_x + 1) \times (N_y + 1)$ where N_x and N_y denote the number of nodes in the x and y directions, respectively. We employ the second-order finite difference scheme with five-point stencil to approximate the equation and the boundary conditions. In this work, we consider only the rectangular domain, defined by $[x_{min}, x_{max}] \times [y_{min}, y_{max}]$. Define $\Delta x = \frac{1}{N_x}$ and $\Delta y = \frac{1}{N_y}$. The spatial steps are marked in Δx and Δy . We switch the notations so that $u_{m,j} = u(x_{min} + m\Delta x, y_{min} + j\Delta y)$, where $m = 0, \dots, N_x$ ($N_x\Delta x = x_{max}$) and $j = 0, \dots, N_y$ ($N_y\Delta y = y_{max}$). Same for the spatially dependent wave number and forcing function $k_{m,j}$ and $f_{m,j}$ respectively. The differential equation is discretized as:

$$\begin{aligned} \frac{u_{m+1,j} - 2u_{m,j} + u_{m-1,j}}{\Delta x^2} + \frac{u_{m,j+1} - 2u_{m,j} + u_{m,j-1}}{\Delta y^2} + k_{m,j}^2 u_{m,j} &= \left(\frac{1}{\Delta x^2}\right) u_{m+1,j} + \\ \left(\frac{1}{\Delta x^2}\right) u_{m-1,j} + \left(\frac{1}{\Delta y^2}\right) u_{m,j+1} + \left(\frac{1}{\Delta y^2}\right) u_{m,j-1} + \left(k_{m,j}^2 - \frac{2}{\Delta x^2} - \frac{2}{\Delta y^2}\right) u_{m,j} &= f_{m,j}. \end{aligned} \quad (\text{A.1})$$

The left boundary $\frac{\partial u}{\partial x} + iku = 0$ is discretized as:

$$\frac{u_{1,j} - u_{0,j}}{\Delta x} + ik_{0,j} \frac{u_{1,j} + u_{0,j}}{2} = \left(\frac{1}{\Delta x} + \frac{ik_{0,j}}{2}\right) u_{1,j} + \left(-\frac{1}{\Delta x} + \frac{ik_{0,j}}{2}\right) u_{0,j} = 0, \quad (\text{A.2})$$

the right boundary $\frac{\partial u}{\partial x} - iku = 0$:

$$\frac{u_{N_x,j} - u_{N_x-1,j}}{\Delta x} - ik_{N_x,j} \frac{u_{N_x,j} + u_{N_x-1,j}}{2} = \left(\frac{1}{\Delta x} - \frac{ik_{N_x,j}}{2}\right) u_{N_x,j} + \left(-\frac{1}{\Delta x} - \frac{ik_{N_x,j}}{2}\right) u_{N_x-1,j} = 0, \quad (\text{A.3})$$

the bottom boundary $\frac{\partial u}{\partial y} + iku = 0$:

$$\frac{u_{m,1} - u_{m,0}}{\Delta y} + ik_{m,0} \frac{u_{m,1} + u_{m,0}}{2} = \left(\frac{1}{\Delta y} + \frac{ik_{m,0}}{2}\right) u_{m,1} + \left(-\frac{1}{\Delta y} + \frac{ik_{m,0}}{2}\right) u_{m,0} = 0, \quad (\text{A.4})$$

and the top boundary $\frac{\partial u}{\partial y} = g$:

$$\frac{u_{m,N_y} - u_{m,N_y-1}}{\Delta y} = \left(\frac{1}{\Delta y}\right) u_{m,N_y} - \left(\frac{1}{\Delta y}\right) u_{m,N_y-1} = g_m. \quad (\text{A.5})$$

In the case of no incoming wave, a Sommerfeld absorbing boundary condition is imposed at the top boundary $\frac{\partial u}{\partial y} - iku = 0$, discretized as follows:

$$\frac{u_{m,N_y} - u_{m,N_y-1}}{\Delta y} - ik_{m,N_y} \frac{u_{m,N_y} + u_{m,N_y-1}}{2} = \left(\frac{1}{\Delta y} - \frac{ik_{m,N_y}}{2}\right) u_{m,N_y} + \left(-\frac{1}{\Delta y} - \frac{ik_{m,N_y}}{2}\right) u_{m,N_y-1} = 0, \quad (\text{A.6})$$

The discretization is similar in 3D cases, in which the central scheme is employed to approximate the second-order derivative in the equation and the forward scheme is employed to approximate the first-order derivative on the boundary.

	$h = \frac{1}{16}$	$h = \frac{1}{32}$	$h = \frac{1}{64}$	$h = \frac{1}{128}$	$h = \frac{1}{256}$
$u(x, y) = \exp(ik((x - 0.5)^2 + (y - 0.5)^2))$	0.0364	0.0191	0.0098	0.0050	0.0025
$u(x, y) = \exp(ik(x + y))$	0.0315	0.0072	0.0017	0.0004	0.0001

Table B.1: Verification test of the finite difference solver for the 2D complex Helmholtz equation without scatterers. L_1 errors are presented and $k(\vec{x}) = 6, \forall \vec{x} \in \Omega$.

Appendix B. Verification test of the numerical solver

Appendix B.1. Sommerfeld radiation condition

We implement the absorbing boundary condition using the lowest-order approximation to the Sommerfeld radiation condition, see e.g. [39]. Before introducing a scatterer, we verify the correctness of the two-dimensional Helmholtz problem solver for the boundary conditions only. We consider a square domain $\Omega = [0, 1]^2$ and impose $\frac{\partial u}{\partial n} - ik u = 0$ to all the boundaries. We further assume constant wave number $k(x, y) = 6, x, y \in [0, 1]$ and choose $u(x, y) = \exp(ik((x - 0.5)^2 + (y - 0.5)^2))$ so that the solution that satisfies the boundary condition:

1. At the boundary where $x = 0$, we have $\frac{\partial u}{\partial n} = -\frac{\partial u}{\partial x} = -2ik(x-0.5) \exp(ik((x - 0.5)^2 + (y - 0.5)^2)) = iku|_{x=0}$.
2. At the boundary where $x = 1$, we have $\frac{\partial u}{\partial n} = \frac{\partial u}{\partial x} = 2ik(x-0.5) \exp(ik((x - 0.5)^2 + (y - 0.5)^2)) = iku|_{x=1}$.
3. At the boundary where $y = 0$, we have $\frac{\partial u}{\partial n} = -\frac{\partial u}{\partial y} = -2ik(y-0.5) \exp(ik((x - 0.5)^2 + (y - 0.5)^2)) = iku|_{y=0}$.
4. At the boundary where $y = 1$, we have $\frac{\partial u}{\partial n} = \frac{\partial u}{\partial y} = 2ik(y-0.5) \exp(ik((x - 0.5)^2 + (y - 0.5)^2)) = iku|_{y=1}$.

The forcing term f is derived by plugging the analytic solution into the equation:

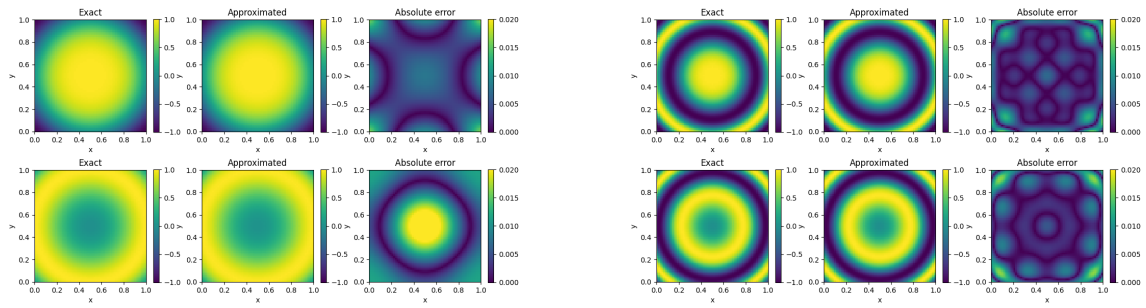
$$\begin{aligned} f &= \Delta u + k^2 u = (2ik - 4k^2(x - 0.5)^2)u + (2ik - 4k^2(y - 0.5)^2)u + k^2 u \\ &= (4ik + k^2 - 4k^2((x - 0.5)^2 + (y - 0.5)^2)) \exp(ik((x - 0.5)^2 + (y - 0.5)^2)). \end{aligned} \quad (\text{B.1})$$

Here, we set $\Delta x = \Delta y = h$ and present the accuracy of the finite difference solver used in this work in Table B.1, from which we observe first-order accuracy of the solver, which is consistent with the first-order scheme used at the boundary.

Besides, we also test the case where the domain is the same and the solution is $\exp(ik(x + y))$, where $k(x, y) = 6, x, y \in [0, 1]$. The boundary condition in this case is: $\frac{\partial u}{\partial n} - ik u = 0$ at the top and right boundaries and $\frac{\partial u}{\partial n} + ik u = 0$ at the bottom and left boundaries. The forcing term is derived by plugging the analytic solution into the equation: $f(x, y) = -k^2 \exp(ik(x + y)), x, y \in [0, 1]^2$. We present the accuracy of the finite difference solver in Table B.1, and results from different wave numbers in Fig. B.13.

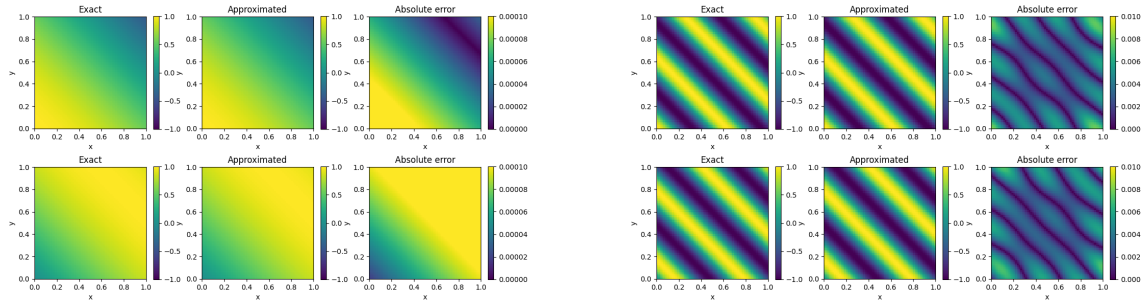
Appendix B.2. The scattering problem

For the scattering problem, we use a setup of the problem where we have an analytic solution to verify the correctness of our finite different solver:



(a) $u(x, y) = \exp(ik((x - 0.5)^2 + (y - 0.5)^2))$ with $k = 6$.

(b) $u(x, y) = \exp(ik((x - 0.5)^2 + (y - 0.5)^2))$ with $k = 20$.



(c) $u(x, y) = \exp(ik(x + y))$ with $k = 1$.

(d) $u(x, y) = \exp(ik(x + y))$ with $k = 10$.

Figure B.13: Examples of solving the 2D Helmholtz equation without scatterers showing the correctness of our solver. The top rows are for the real parts and the bottom rows for the imaginary parts. Note that the wave number k is constant and the forcing term f and the boundary condition are adjusted accordingly to the test solution.

1. The domain is a square $\Omega = [0, 1] \times [0, 1]$ with $N_x = N_y = 32$. We mark the center of the domain Ω by $(x_0, y_0) = (0.5, 0.5)$.
2. The scatterer is a square $\Omega_{scat} = [x_l, x_u] \times [y_l, y_u]$. We choose $x_l = y_l = 0.4375$ and $x_u = y_u = 0.5625$ for this setup.
3. The wave number is taken constant $k(x, y) = 6$.
4. We define a function $d_{\square}(x, y) = \min_{(x_s, y_s) \in \partial\Omega_{scat}} \sqrt{(x - x_s)^2 + (y - y_s)^2}$, that calculates the distance between each point inside the domain $(x, y) \in \Omega$ and the scatterer. The values of d_{\square} on the points inside the scatterer are set to zero.
5. The boundary condition applied on the scatterer boundary is $u(x, y) = 0$, $(x, y) \in \partial\Omega_{scat}$.
6. We define $v = \frac{\psi}{r}$, where $r(x, y) = \sqrt{(x - x_0)^2 + (y - y_0)^2}$, and $\psi \sim H_0(kr) \sim \frac{e^{ikr}}{\sqrt{r}}$ is the Hankel function.
7. The chosen analytic solution for the problem is $u(x, y) = d_{\square}(x, y)v(x, y) = \frac{e^{ikr}}{r^{\frac{3}{2}}}d_{\square}$. In the far-field $u \sim \psi$.

The remaining element is the forcing term $f(x, y)$, which we get by substituting the information of the setup into the problem equations. To compute the exact derivatives we first consider the domain split to eight regions, the different regions of the function d_{\square} . The regions and the values of d_{\square} in each region are shown in Figure B.14. To compute the forcing

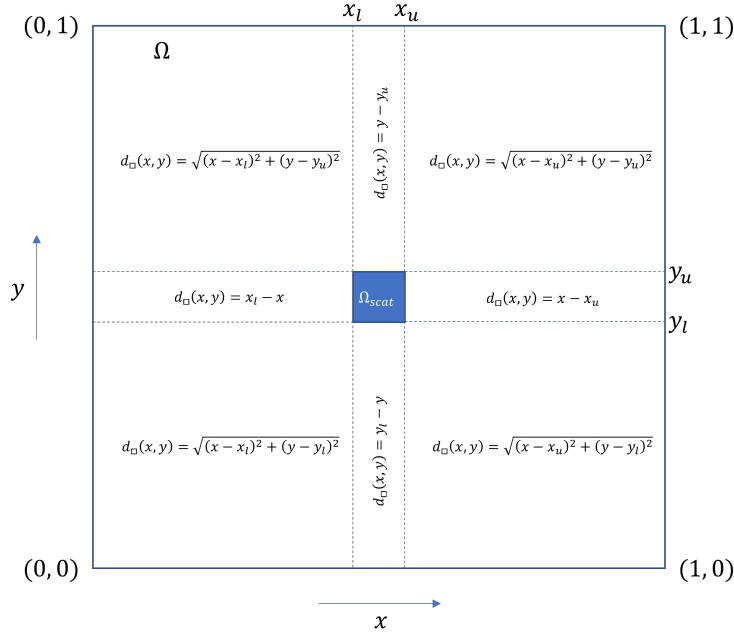


Figure B.14: Splitting the domain into 8 regions around the scatterer. The values of the function $d_{\square}(x, y)$ are different in each region, as shown here.

term we need to compute the Laplacian of u . We use the following:

$$\nabla^2 u(x, y) = \nabla^2 \left(\frac{e^{ikr}}{r^{\frac{3}{2}}} \right) d_{\square} + 2\nabla \left(\frac{e^{ikr}}{r^{\frac{3}{2}}} \right) \cdot \nabla d_{\square} + \left(\frac{e^{ikr}}{r^{\frac{3}{2}}} \right) \nabla^2 d_{\square}. \quad (\text{B.2})$$

Setting $\theta(x, y) = \arctan\left(\frac{y-y_0}{x-x_0}\right)$, we compute each element individually using the first and second gradients in polar coordinates:

$$\begin{aligned}\nabla(\cdot) &= \vec{e}_r \frac{\partial(\cdot)}{\partial r} + \vec{e}_\theta \frac{1}{r} \frac{\partial(\cdot)}{\partial \theta}, \\ \nabla^2(\cdot) &= \frac{1}{r} \frac{\partial}{\partial r} \left(r \frac{\partial(\cdot)}{\partial r} \right) + \frac{1}{r^2} \frac{\partial^2(\cdot)}{\partial \theta^2} = \frac{1}{r} \frac{\partial(\cdot)}{\partial r} + \frac{\partial^2(\cdot)}{\partial r^2} + \frac{1}{r^2} \frac{\partial^2(\cdot)}{\partial \theta^2}.\end{aligned}$$

Where \vec{e}_r and \vec{e}_θ are unit vectors in the directions of r and θ respectively. We start with the function $v(x, y)$, since it does not involve splitting to different parts of the domain. Computing the derivatives we get:

$$\begin{aligned}\nabla \frac{e^{ikr}}{r^{\frac{3}{2}}} &= \vec{e}_r \left(\frac{\partial}{\partial r} \frac{e^{ikr}}{r^{\frac{3}{2}}} \right) = \vec{e}_r \frac{ikr - \frac{3}{2}}{r^{\frac{5}{2}}} e^{ikr} = \\ &= (\cos \theta \vec{e}_x + \sin \theta \vec{e}_y) \frac{ikr - \frac{3}{2}}{r^{\frac{5}{2}}} e^{ikr} = \underbrace{\cos \theta \frac{ikr - \frac{3}{2}}{r^{\frac{5}{2}}} e^{ikr}}_{\frac{\partial}{\partial x} \left(\frac{e^{ikr}}{r^{\frac{3}{2}}} \right)} \vec{e}_x + \underbrace{\sin \theta \frac{ikr - \frac{3}{2}}{r^{\frac{5}{2}}} e^{ikr}}_{\frac{\partial}{\partial y} \left(\frac{e^{ikr}}{r^{\frac{3}{2}}} \right)} \vec{e}_y,\end{aligned}\quad (\text{B.3})$$

$$\begin{aligned}\nabla^2 \frac{e^{ikr}}{r^{\frac{3}{2}}} &= \frac{1}{r} \left(\frac{\partial}{\partial r} \frac{e^{ikr}}{r^{\frac{3}{2}}} \right) + \left(\frac{\partial^2}{\partial r^2} \frac{e^{ikr}}{r^{\frac{3}{2}}} \right) + \frac{1}{r^2} \left(\frac{\partial^2}{\partial \theta^2} \frac{e^{ikr}}{r^{\frac{3}{2}}} \right) = \\ &= \frac{1}{r} \frac{ikr - \frac{3}{2}}{r^{\frac{5}{2}}} e^{ikr} + \left(-3ikr - k^2 r^2 + \frac{15}{4} \right) \frac{e^{ikr}}{r^{\frac{7}{2}}} = \left(-2ikr - k^2 r^2 + \frac{9}{4} \right) \frac{e^{ikr}}{r^{\frac{7}{2}}}.\end{aligned}\quad (\text{B.4})$$

Where \vec{e}_x and \vec{e}_y are unit vectors in the directions x and y respectively. For the derivatives of d_\square , we split the computations according to the eight regions. We show the derivatives computations of the top right region (where $x > x_u$ and $y > y_u$) and the flat region below it (where $x > x_u$ and $y_l < y \leq y_u$, see Figure B.14). In the other regions, similar computations are performed but with minus signs and different constants (x_l, x_u, y_l, y_u). In the top right region, we have:

$$\begin{aligned}d_\square(x, y)|_{\substack{x > x_u \\ y > y_u}} &= \sqrt{(x - x_u)^2 + (y - y_u)^2} \\ \theta_\square(x, y)|_{\substack{x > x_u \\ y > y_u}} &= \arctan\left(\frac{y - y_u}{x - x_u}\right)\end{aligned}$$

The derivatives are:

$$\nabla d_\square|_{\substack{x > x_u \\ y > y_u}} = \frac{\partial d_\square}{\partial x} \vec{e}_x + \frac{\partial d_\square}{\partial y} \vec{e}_y = \frac{x - x_u}{d_\square} \vec{e}_x + \frac{y - y_u}{d_\square} \vec{e}_y = \vec{e}_{d_\square} = \cos(\theta_\square) \vec{e}_x + \sin(\theta_\square) \vec{e}_y, \quad (\text{B.5})$$

$$\nabla^2 d_\square|_{\substack{x > x_u \\ y > y_u}} = \frac{1}{d_\square}. \quad (\text{B.6})$$

For the flat region below the top right region, we have $d_\square(x, y)|_{\substack{x > x_u \\ u_l < y \leq y_u}} = x - x_u$ and the derivatives are:

$$\nabla d_\square|_{\substack{x > x_u \\ u_l < y \leq y_u}} = \vec{e}_x, \quad (\text{B.7})$$

$$\nabla^2 d_\square|_{\substack{x > x_u \\ u_l < y \leq y_u}} = 0. \quad (\text{B.8})$$

$h = \frac{1}{16}$	$h = \frac{1}{32}$	$h = \frac{1}{64}$	$h = \frac{1}{128}$	$h = \frac{1}{256}$
0.4522	0.2428	0.1286	0.0676	0.0351

Table B.2: Verification test of the finite difference solver for the 2D complex Helmholtz equation with a square scatterer. L_1 errors are presented and $k(\vec{x}) = 6, \forall \vec{x} \in \Omega$.

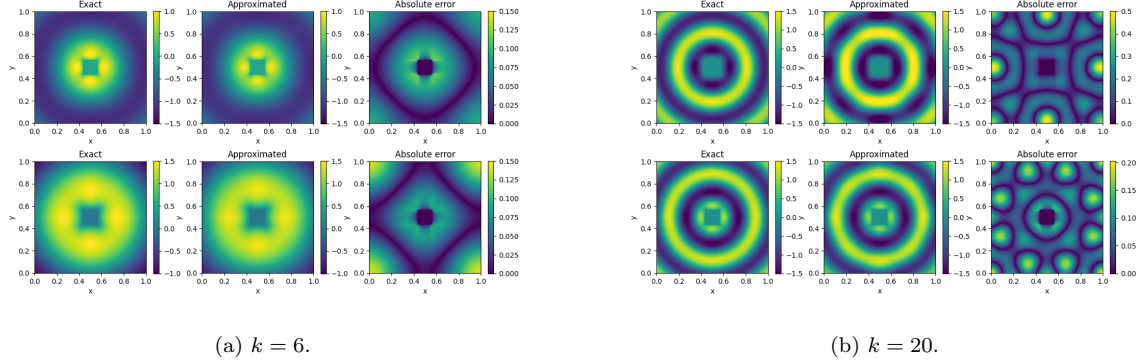


Figure B.15: Examples of solving the 2D Helmholtz equation with a square scatterer showing the correctness of our solver in solving the scattering problem. The top rows are for the real parts and the bottom rows are for the imaginary parts. Note that the wave number k is constant and the forcing term f and the boundary condition are adjusted accordingly to the test solution.

Using Eqs. (B.3) and (B.5) we compute the cross term in the top right region:

$$\nabla \left(\frac{e^{ikr}}{r^{\frac{3}{2}}} \right) \cdot \nabla d_{\square} \Big|_{\substack{x > x_u \\ y > y_u}} = \cos \theta \frac{ikr - \frac{3}{2}}{r^{\frac{5}{2}}} e^{ikr} \cos(\theta_{\square}) + \sin \theta \frac{ikr - \frac{3}{2}}{r^{\frac{5}{2}}} e^{ikr} \sin(\theta_{\square}), \quad (\text{B.9})$$

and using Eqs. (B.3) and (B.7) in the flat region:

$$\nabla \left(\frac{e^{ikr}}{r^{\frac{3}{2}}} \right) \cdot \nabla d_{\square} \Big|_{\substack{x > x_u \\ u_l < y \leq y_u}} = \cos \theta \frac{ikr - \frac{3}{2}}{r^{\frac{5}{2}}} e^{ikr}. \quad (\text{B.10})$$

We then compute the forcing term in the top right region by plugging Eqs. (B.4), (B.6), and (B.9) into Eq. (B.2) and using $f(x, y) = \nabla^2 u(x, y) + k^2(x, y)u(x, y)$. The same for the other regions. In addition, we compute the boundary values by $g(x, y) = \frac{\partial u}{\partial \mathbf{n}} = \frac{e^{ikr}}{r^{\frac{3}{2}}} \nabla d_{\square} + \frac{\partial}{\partial \mathbf{n}} \left(\frac{e^{ikr}}{r^{\frac{3}{2}}} \right) d_{\square}$ for all the edges (\mathbf{n} is the normal direction to the edge). For each direction (x or y) we use Eq. (B.3) for the derivatives.

We use the solver developed to approximate the solution of this scattering problem and compare it to the analytic solution to verify the correctness of the numerical solver.

Appendix C. Details of data generation and the training of neural operators (NOs)

In this section, we present additional details of the numerical examples, including data generation, the architecture of DeepONets, and their training. In this work, the Adam optimizer [50] with a constant learning rate 1×10^{-4} is used to train DeepONets, and the PyTorch module [51] is used for machine learning related computation.

Appendix C.1. 2D scattering problems

In Section 4.1, the 2D Gaussian random field (GRF) from which samples of the wave number $k(x, y)$ are drawn has mean six and kernel function (3) with $l = 0.3$ and $s = 0.5$. The 1D GRF for the incoming wave $g(x)$ has mean zero and kernel function (3) with $l = 0.1$ and $s = 1$. For the forcing term $f(x, y)$, since it is a complex-valued function, samples of its real part and samples of its imaginary part are drawn independently from the same 2D GRF, which has mean zero and kernel function (3) with $l = 0.1$ and $s = 1$. For the training of NOs, we take 20,000 samples of k , f , and g , and solve the 2D complex Helmholtz equation to obtain the data of u . For the NO on non-scattering problems, the data of u are obtained by solving Eq. (1) with $\Omega_{scat} = \emptyset$, while for the NO on scattering problems, the data of u are obtained by solving Eq. (1) with $\Omega_{scat} = [0.4375, 0.5625]^2$ and associated Dirichlet boundary condition. We note that the forcing term is not assumed to be zero in the training of NOs, because the NO approximates the solution operator of the complex Helmholtz equation. However, for the physical scattering problem described by the Helmholtz equation, the forcing term is set equal to zero.

Recall that in this work, the NO employed in HINTS consists of two DeepONets: DeepONet 1 takes as input the wave number and the forcing term, and DeepONet 2 takes as input the wave number and the incoming wave. In Section 4.1, the branch net of DeepONet 1 is a 2D convolutional neural network (CNN) (input dimension 33×33 , channels number [3, 40, 60, 100, 180], kernel size 3×3 , stride 2×2 , valid padding, ReLU activation function) followed by a fully-connected neural network (FNN) (width [180, 256, 256, 160], ReLU activation function for all hidden layers). Its trunk net is a FNN (width [2, 80, 80, 80, 160], Leaky ReLU activation function). The trunk net of DeepONet 2 has the same architecture as the one of DeepONet 1. As for its branch net, it only differs in the first channel number: it is 2 instead of 3. In both DeepONets, the input to the trunk net is \vec{x} , which is two-dimensional. The input to the branch is the concatenation of the values of the wave number and the real and imaginary parts of the forcing term on a mesh in DeepONet 1. In DeepONet 2, the input is the concatenation of the values of the wave number and \tilde{g} on a mesh. Here \tilde{g} is defined as $\tilde{g}(x, y) := g(x), \forall x, y$. NOs in Section 4.1 are trained for 30,000 epochs with batch size 1000.

Appendix C.2. 3D scattering problems

In Section 4.2, the 3D Gaussian random field (GRF) from which samples of the wave number $k(x, y, z)$ are drawn has mean six and kernel function (3) with $l = 0.3$ and $s = 0.2$. Similarly, we reject samples of k whose minimal values are smaller than or equal to three to ensure that the wave number is not too small. The 2D GRF for the incoming wave $g(x, y)$ has mean zero and kernel function (3) with $l = 0.1$ and $s = 1$. The 3D GRFs for the real and imaginary parts of the forcing term $f(x, y, z)$ have mean zero and kernel function (3) with $l = 0.1$ and $s = 1$. For the training of NOs, we take 30,000 samples of k , f , and g , and solve the 3D complex Helmholtz equation without the scatterer (Eq. (1) with $\Omega_{scat} = \emptyset$) to obtain the data of u . Recall that we only have one NO in Section 4.2.

For the DeepONet which takes as input the wave number and the forcing term (DeepONet 1), its branch net is a 3D CNN (input dimension $17 \times 17 \times 17$, channels number [3, 40, 40, 60], kernel size 3×3 , stride 2×2 , same padding in the second convolutional layer and valid padding in the rest, ReLU activation function) followed by a FNN (width [1620, 1000, 1000, 1000], ReLU activation function for all hidden layers). Its trunk net is a

FNN (width [3, 1000, 1000, 1000, 1000], Leaky ReLU activation function for all hidden layers). For the DeepONet which takes as input the wave number and the incoming wave (DeepONet 2), its trunk net has the same architecture as the one in the other DeepONet. Its branch net differs in the first channel number compared with the one in the other DeepONet: it is 2 instead of 3. In both DeepONets, the input to the trunk net is \vec{x} , which is three-dimensional. The input to the branch is the concatenation of the values of the wave number and the real and imaginary parts of the forcing term on a mesh in DeepONet 1. In DeepONet 2, the input is the concatenation of the values of the wave number and \tilde{g} on a mesh. Here \tilde{g} is defined as $\tilde{g}(x, y, z) := g(x, y), \forall x, y, z$. The NO in Section 4.2 is trained for 10,000 epochs with batch size 500.